(will be inserted by hand later)

The phase-diagram of cosmological baryons

P. Valageas[1], R. Schaeffer[1], and J. Silk[2]

[1] Service de Physique Théorique, CEN Saclay, 91191 Gif-sur-Yvette, France
[2] Astrophysics, Department of Physics, Keble Road, Oxford OX1 3RH, UK

Received / Accepted

Abstract. We investigate the behaviour of cosmological baryons at low redshifts $z \lesssim 5$ after reionization through analytic means. In particular, we study the density-temperature phase-diagram which describes the history of the gas. Thus, we show how the location of the matter in this (ρ, T) diagram expresses the various constraints implied by usual hierarchical scenarios. This yields robust model-independent results which agree with numerical simulations. Thus, the IGM is seen to be formed by two phases: a "cool" photo-ionized component and a "warm" component governed by shock-heating. We recover the fraction of matter and the spatial clustering computed by numerical simulations. We also check that the soft X-ray background due to the "warm" IGM component is consistent with observations.

Key words. cosmology: theory – large-scale structure of Universe – galaxies: intergalactic medium

1. Introduction

As is well known, the mass of baryons embedded within stars or galactic disks in the current universe is quite small since it yields a baryonic parameter $\Omega_{\rm gal} \sim 0.002 - 0.006$ (e.g., Fukugita et al. (1998)) (we always use a Hubble constant $H_0 = 65$ km/s/Mpc in this paper) while standard nucleosynthesis calculations give $\Omega_{\rm b} \simeq 0.045$ (e.g., Tytler et al. (2000)). Therefore, most of the baryonic matter should lie in the intergalactic medium. This agrees rather well with the fact that at higher redshift one observes a large amount of mass in the Lyman-α forest which consists of moderate density fluctuations ionized by the background UV flux emitted by distant galaxies. Thus, one gets $\Omega_{{\rm Ly}\alpha} \sim 0.01 - 0.05$ at $z \sim 3$ (e.g., Fukugita et al. (1998)). However, as noticed in Cen & Ostriker (1999) the mass within the Lyman-α forest decreases with time and at $z = 0$ summing over all observed contributions one obtains $\Omega_{\rm b} \lesssim 0.011$ which falls short of the required total baryonic mass. Hence at $z = 0$ a large part of the baryons must lie in a new intergalactic component beyond the usual Lyman-α forest clouds. As argued in Cen & Ostriker (1999) and Dave et al. (2001) this could be part of in the form of a "warm" phase of the intergalactic medium (IGM), with temperatures in the range $10^5 < T < 10^7$ K.

The latter conclusion was reached from numerical simulations. In this article, we reconsider this problem in order to derive the properties of the IGM by analytic means. In particular, we wish to investigate whether one can understand this behaviour in a quantitative manner from robust, model-independent, arguments. First, in Sect.2 we study the (ρ, T) phase-diagram of cosmological baryons. While the Lyman-α forest is described by a well-defined Equation of State the "warm" IGM component shows a broad scatter (e.g., Dave et al. (1999), Dave et al. (2001)) since its temperature depends through shock-heating on the neighbouring gravitational potential which is a stochastic field. Nevertheless, we show that it is constrained to lie in a well-defined domain in the (ρ, T) plane, and determine its average location in this plane, which may be considered as the "Equation of State" of the warm IGM.

Next, in Sect.3 we use our result to compute the redshift evolution of the fraction of matter enclosed within the "cool" IGM phase which corresponds to the Lyman-α forest. Then, in Sect.4 we estimate the two-point correlation function and the clumping factor of the "warm" IGM. Finally, in Sect.5 we check that the X-ray background emitted by the "warm" component agrees with observations.

2. The phase-diagram of cosmological baryons

In this section we investigate the evolution of the physical properties of the baryons at moderate redshifts $z \lesssim 5$, as gravitational clustering builds up. To do so, we study the distribution of matter in a density-temperature plane and determine the (ρ, T) phase-diagram. Indeed, as we describe below baryons are located within specific regions in this (ρ, T) plane which reflect the various processes (cooling, radiative heating, shock-heating, gravitational clus-

tering,...) which take place in the universe. We display our results in Fig.1. Note that we use the overdensity $1+\delta = \rho/\overline{\rho}$ rather than the density ρ in the figures, where $\overline{\rho}$ is the mean density of the universe.

In this article, all our numerical results are obtained with the following cosmological parameters. We consider a low-density flat universe with $\Omega_{\rm m} = 0.4$ and $\Omega_\Lambda = 0.6$. The baryonic density parameter is $\Omega_{\rm b} = 0.0473$ and the Hubble constant is $H_0 = 65$ km/s/Mpc. The ΛCDM power-spectrum of the linear density fluctuations is normalized by $\sigma_8 = 0.8$.

2.1. Temperature-scale relation of warm halos

We consider two processes for the possible heating of the gas. First, the gas temperature may be governed by a local shock-heating due to gravitational processes. Thus, as large-scale structures build up we expect tidal effects and virialization processes to heat the gas within and in the neighbourhood of collapsed halos up to the virial temperature of the underlying gravitational potential well. The latter scales as $\Phi \sim \mathcal{G}\rho R^2$, which defines the characteristic scale R, hence we write:

$$\text{local heating}: \quad kT = \frac{8\pi}{9}\mu m_p \mathcal{G}\rho R^2, \tag{1}$$

where μm_p is the mean molecular weight of the gas and m_p the proton mass.

Second, the gas temperature may be set by an external heating source, like a UV background radiation. Then, the temperature is no longer given by eq.(1) since it is not fixed by the virial temperature of a neighbhouring halo. However, the pressure of the gas erases the baryonic density fluctuations over a scale R given by:

$$\text{external heating}: \quad R = t_H C_s = t_H \sqrt{\frac{\gamma kT}{\mu m_p}}, \tag{2}$$

where C_s is the sound velocity and $\gamma = 5/3$. This is simply the distance over which sound waves can travel in a Hubble time and build pressure equilibrium. Therefore, the gas sees the dark matter density field smoothed over this scale R.

There is a characteristic density ρ_c at which shock heating starts to play a role, that is where eq.(1) is to be used in place of eq.(2). It is expected to correspond to a density contrast of a few units at least. The detailed discussion of the relation between the two regimes around $\rho \sim \rho_c$ may be found in Sect.2.4 below.

2.2. Exclusion constraints

First, we note that the distribution of matter in the (ρ, T) plane is strongly constrained by the existence of some exclusion regions where no particles can be found. The advantage of such conditions is that they are very robust in the sense they do not depend on the detailed history of the baryons. Therefore, they should apply to any hierarchical scenario of structure formation. Then, they provide a first guideline for the properties of baryons. We discuss these various constraints in the sections below. For sake of clarity, we turn within the diagrams shown in Fig.1 in counter-clockwise order.

2.2.1. Cooling constraint

Thus, the dashed-line on the far-right with an inclined "V-shape" is the familiar cooling constraint (see also Rees & Ostriker (1977), Silk (1977)). It expresses the fact that high-density ionized hot gas ($T > 10^4$ K) cools very rapidly. Thus, baryons cannot remain for long in regions located to the right of this dashed-line. More precisely, we write the local energy equation as:

$$\frac{{\rm d}e}{{\rm d}t} = -\frac{e}{t_{\rm cool}} + \frac{e}{t_{\rm heat}} + \frac{e}{t_{\rm grav}} \equiv -\frac{e}{t_{\rm c,ef}} \tag{3}$$

where $e = 3/2 n_b kT$ is the specific energy and n_b is the baryon number density. The cooling time $t_{\rm cool}$ describes collisional excitation, collisional ionization, recombination, molecular hydrogen cooling, bremsstrahlung and Compton cooling or heating (e.g., Anninos et al. (1997)). The heating time $t_{\rm heat}$ is the radiative heating time due to a UV background radiation of the form $J_\nu \propto \nu^{-1}$. As usual, we normalize the UV flux by its value J_{21} at the HI ionization threshold ($912\mathring{A}$) in units of 10^{-21} erg s^{-1} Hz^{-1} cm^{-2} sr^{-1}. The values we choose for J_{21} are given in Tab.1 as a function of redshift. They are consistent with observations (e.g., Giallongo et al. (1996), Cooke et al. (1997), Vogel et al. (1995)) and are the same as the ones used for modeling the evolution of Lyman-α clouds Valageas et al. (1999). The time-scale $t_{\rm grav}$ in eq.(3) corresponds to shock-heating due to gravitational processes (e.g., virialization). We simply take $t_{\rm grav} = t_H$ where t_H is the Hubble time. This is the time-scale over which new structures form. Finally, $t_{\rm c,ef}$ is the "effective" cooling time, which is defined by eq.(3). Then, the cooling curve shown in Fig.1 is given by the condition:

$$\text{cooling}: \quad t_{\rm c,ef} = t_H. \tag{4}$$

Note that this constraint is actually quite robust as $t_{\rm c,ef}$ mainly depends on the cooling time $t_{\rm cool}$. That is, the location of the cooling curve does not depend much on the times $t_{\rm heat}$ and $t_{\rm grav}$. Besides, since it only involves high-density regions ($\delta \gtrsim 30$) which have already turned non-linear and collapsed, we do not need to take into account the expansion of the universe (which would operate on the time-scale t_H in any case). Then, the regions located to the right of the cooling curve have a cooling time which is less than the Hubble time. Hence no particle can remain in this part of the (ρ, T) plane for a Hubble time. This process is actually at the origin of galaxy formation as this gas cools and falls to the center of the gravitational well to form a disk and stars (e.g., Valageas & Schaeffer (1999)). This means that the matter which entered this region at some time should accumulate on the lower branch of the cooling curve (at $T \sim 10^4$ K) under the form of high-density cool

Table 1. Redshift evolution of the background UV flux $J_{21}(z)$ used in this article.

z =0	1	2	3	4	5
$J_{21} = 0.05$	0.5	0.8	0.4	0.2	0.1

gas which evolves on a Hubble time. Some of this gas also turns into stars but we do not study this latter process in this article. Note that this accumulation of baryons along the lower branch is clearly seen in the numerical simulations displayed in Fig.11 in Dave et al. (1999) and in Fig.9 in Springel & Hernquist (2001).

2.2.2. High-density fluctuations

A second constraint is set by the properties of the dark matter density field itself. Indeed, at a given scale R beyond some threshold $\rho_+(R)$ large densities have a negligible probability and only involve a very small amount of matter. In the linear regime for instance, at large scales R, the probability distribution function (pdf) $P(\delta_R)$ of the density contrast δ_R over a spherical cell of radius R is a Gaussian of variance $\sigma(R)$. Here we note as usual $\sigma(R)$ the rms linear density fluctuation and we assume Gaussian initial density fluctuations. In the non-linear regime, for highly non-Gaussian probabilities, the analogue of this upper threshold can also be calculated. It is given in App.A where we detail our model for the pdf $P(\rho_R)$, where $\rho_R = 1 + \delta_R$ is the overdensity. The high-density cutoff defined by eq.(A.8) obeys the asymptotic behaviour (A.10) in the quasi-linear and highly non-linear regimes. Note that this asymptotic behaviour actually is model-independent. Indeed, in the limit $\overline{\xi} \ll 1$ we recover the Gaussian cutoff implied by the initial conditions (where $\overline{\xi} = \langle \delta_R^2 \rangle$). On the other hand, in the limit $\overline{\xi} \gg 1$ we recover the fact that most of the matter is enclosed within high-density halos of density contrast $\delta_R \sim \overline{\xi}$ which occupy a small fraction of the volume ($\sim 1/\overline{\xi}$) of the universe. Therefore, the constraint given by the high-density cutoff of the pdf $P(\rho_R)$ in the (ρ, T) plane is quite robust and it applies to all hierarchical scenarios of structure formation.

Then, assuming that the baryon density ρ_b scales as the dark matter density through:

$$\rho_b = \frac{\Omega_{\rm b}}{\Omega_{\rm m}} \rho, \tag{5}$$

which should be valid out of the cooling region discussed above in Sect.2.2.1, we obtain an upper cutoff for the baryon overdensity $\rho_+(R)$ at any given scale R. Next, we need to express the cutoff $\rho_+(R)$ in terms of a density-temperature relation, in order to draw its consequences for the phase-diagram (ρ, T) of the IGM. To do so we simply need a relation $T(\rho, R)$.

Substituting eq.(1) into the relation $\rho_+(R)$ derived in eq.(A.8) we obtain a curve $\rho_{+,\rm loc}(T)$. The subscript "loc" in the overdensity cutoff $\rho_{+,\rm loc}$ refers to the fact that this is a "local" heating process. It is due to the gravitational interaction with neighbouring structures. This high-density cutoff $\rho_{+,\rm loc}(T)$ corresponds to the dot-dashed curve shown in the diagrams in Fig.1 which runs from $\delta \sim 5$ up to $\delta \sim 10^4$ and which crosses the cooling curve.

Substituting eq.(2) into the relation $\rho_+(R)$ obtained from eq.(A.8) we get a curve $\rho_{+,\rm ext}(T)$. This corresponds in Fig.1 to the short branch which runs upward from the curve $\rho_{+,\rm loc}(T)$ at $\delta \sim 10$. Indeed, we note that for $\delta \gtrsim 10$ the gas is located close to non-linear structures so that local shock-heating must be taken into account. However, for large densities we have $T_{\rm loc} > T_{\rm ext}$ since eq.(2) yields $T_{\rm ext} \sim \mathcal{G}\overline{\rho} R^2$. In this case external heating plays no role. This is why we only plot the curve $\rho_{+,\rm ext}(T)$ up to the characteristic density contrast δ_c where $T_{\rm loc} = T_{\rm ext}$. At higher densities the threshold $\rho_{+,\rm ext}(T)$ becomes irrelevant. In fact, we see in Fig.1 that the curve $\rho_{+,\rm ext}(T)$ due to external heating plays no role since at moderate densities $\rho \sim \overline{\rho}$ it is repelled to quasi-linear scales (see Sect.2.2.3).

Then, the region to the upper-right of the curves $\rho_{+,\rm loc}(T)$ and $\rho_{+,\rm ext}(T)$ in the (ρ, T) plane shown in Fig.1 corresponds to rare high-density fluctuations which are located in the tail of the pdf $P(\rho_R)$. Therefore, there should be very few particles beyond these lines. Thus, this defines a second exclusion region. We shall again encounter the characteristic density ρ_c defined in eq.(22) in Sect.2.3 below, where we discuss the photo-ionization heating of the IGM by the background UV flux. Indeed, it will still mark the transition between this external heating source and local gravitational heating.

2.2.3. Transition to non-linearity

A characteristic scale which enters the problem we investigate here is set by the transition to the non-linear regime. At a given epoch, we define this scale $R_0(z)$ by the relation:

$$\overline{\xi}(R_0, z) \equiv 1. \tag{6}$$

Thus, scales larger than R_0 are still within the linear regime. Then, there can be no shock-heating due to gravitational clustering on these large scales which have not turned non-linear yet. Using eq.(1) we obtain a characteristic temperature $T_{\rm nl}(\rho)$:

$$\text{transition to non-linearity}: \quad kT_{\rm nl} = \frac{8\pi}{9} \mu m_p \mathcal{G} \rho R_0^2, \tag{7}$$

which describes the transition to non-linear scales (which lie at $T \ll T_{\rm nl}(\rho)$). This is shown by the straight dashed-line ($T_{\rm nl} \propto \rho$) plotted in Fig.1. Besides, we note that known sources of external heating (e.g., the UV background radiation) cannot heat the IGM up to such high temperatures. Therefore, the region to the upper-left of the curve $T_{\rm nl}(\rho)$ should be void of matter. This yields a third exclusion region.

2.2.4. Low-density fluctuations

Finally, a fourth constraint on the distribution of matter is given by the low-density cutoff of the pdf $P(\rho_R)$ of the dark matter density field. This is the analog of the high-density cutoff discussed in Sect.2.2.2. The low-density cutoff $\rho_-(R)$ is derived in App.A, from eq.(A.8). It obeys the asymptotic behaviours (A.11). In the quasi-linear regime we again recover the usual Gaussian cutoff $\delta_- \sim -\sigma$. In the highly non-linear regime the small overdensity $\rho_- \sim \overline{\xi}^{-\kappa/2} \ll 1$ expresses the formation of extreme underdensities on small scales. Contrary to the high-density cutoff it is somewhat model-dependent through the exponent κ but this has no strong effect on the (ρ, T) phase-diagram. As in Sect.2.2.2 we need a relation $T(R)$ in order to derive a condition of the form $\rho_-(T)$. We again consider both cases of local and external heating, described by eq.(1) and eq.(2). This yields the curves $\rho_{-,\rm loc}(T)$ and $\rho_{-,\rm ext}(T)$ shown by the two steep parallel dashed-lines in Fig.1, at $\rho_R \sim 10^{-1}$. The curve associated with external heating is the left one (i.e. lower densities or higher temperature), as can be seen from eq.(1) and eq.(2). Thus, this defines a fourth exclusion region to the left of these curves.

2.3. Equation of State of the Lyman-α forest

Thus, so far we have obtained constraints on the distribution of matter in the (ρ, T) plane by drawing four exclusion regions. This already gives some useful information about the properties of the IGM which are very robust. Now, we investigate a different point of view which allows us to derive the location of some of the gas in the (ρ, T) plane. This amounts to deriving an Equation of State for this component.

As shown in Hui & Gnedin (1997) the low-density photo-ionized IGM exhibits such an Equation of State as the gas follows a specific relation $T_\alpha(\rho)$ with a rather small scatter. This was derived in Hui & Gnedin (1997) from the Zel'dovich approximation (Zel'dovich (1970)) which applies up to the moderately non-linear regime ($\overline{\xi} \lesssim 1$). Here we reconsider this problem and we show that this Equation of State is rather robust with respect to the past history of the gas and applies beyond the validity of the Zel'dovich approximation. First, we assume photo-ionization equilibrium (we restrict ourselves to $z \lesssim 5$ after reionization) and we only take into account Hydrogen. Therefore, the ionization equilibrium reads:

$$\Gamma\, n_{\rm HI} = \alpha(T)\, n_{\rm HII} n_e, \tag{8}$$

where Γ is the photo-ionization rate and $\alpha(T)$ is the recombination rate. They are given by:

$$\Gamma = \int 4\pi J_\nu \sigma_{\rm HI} \frac{{\rm d}\nu}{h\nu} = 3.08\times 10^{-12}\ J_{21}(z)\ {\rm s}^{-1} \tag{9}$$

and:

$$\alpha(T) = \alpha_J \left(\frac{T}{T_J}\right)^{-(\nu-1)}, \tag{10}$$

where we defined:

$$\nu = 1.7,\ \alpha_J = 1.23\times 10^{-13}\ {\rm cm^3 s^{-1}},\ T_J = 5.8\times 10^4 {\rm K}. \tag{11}$$

The temperature T_J we introduced in eq.(11) is the characteristic temperature reached by the gas through the heating due to the UV background radiation flux. It is given by:

$$kT_J \equiv \frac{\int 4\pi J_\nu \sigma_{\rm HI}(h\nu - h\nu_{\rm HI})\frac{{\rm d}\nu}{h\nu}}{\int 4\pi J_\nu \sigma_{\rm HI}\frac{{\rm d}\nu}{h\nu}} \simeq 5\ {\rm eV}, \tag{12}$$

where $h\nu_{HI} = 13.6$ eV is the Hydrogen ionization threshold. Note that this temperature T_J does not depend on the amplitude J_{21} of the UV background. Moreover, it is fixed by atomic physics, independently of cosmological parameters. Next, the temperature T of a given fluid element evolves as:

$$\frac{1}{T}\frac{{\rm d}T}{{\rm d}t} = \frac{2}{3}\frac{1}{\rho}\frac{{\rm d}\rho}{{\rm d}t} + \frac{1}{t_{\rm heat}} \tag{13}$$

where ${\rm d}/{\rm d}t$ is the Lagrangian time derivative. The heating time $t_{\rm heat}$ is given by:

$$\begin{aligned}\frac{3/2 n_b kT}{t_{\rm heat}} &= \int 4\pi J_\nu \sigma_{\rm HI} n_{\rm HI}(h\nu - h\nu_{\rm HI})\frac{{\rm d}\nu}{h\nu} \\ &= kT_J n_{\rm HI}\Gamma,\end{aligned} \tag{14}$$

where we take $n_b = 2\rho/m_p$ since we approximate the gas as fully ionized Hydrogen. The evolution eq.(13) is the same as in eq.(3), except that we neglect cooling (which is justified here since we consider here moderate densities and temperatures) and gravitational shock-heating which is irrelevant. On the other hand, the term ${\rm d}\rho/{\rm d}t$ represents the pressure work, which takes into account the expansion of the fluid element. Substituting eq.(14) into eq.(13) we obtain:

$$\frac{1}{T}\frac{{\rm d}T}{{\rm d}t} = \frac{2}{3}\frac{1}{\rho}\frac{{\rm d}\rho}{{\rm d}t} + \frac{1}{t_{10}}\frac{\rho}{\rho_J}\left(\frac{T}{T_J}\right)^{-\nu} \tag{15}$$

where we defined:

$$\rho_J = 3\frac{\Omega_{\rm m}}{\Omega_{\rm b}}\frac{m_p}{\alpha_J t_{10}} \simeq 1.1\times 10^{-28}\ {\rm g\ cm^{-3}} \tag{16}$$

and:

$$t_{10} = 10^{10}\ {\rm years}. \tag{17}$$

Next, it is convenient to introduce the specific entropy s which we define by:

$$s \equiv \frac{T}{T_J}\left(\frac{\rho}{\rho_J}\right)^{-2/3}. \tag{18}$$

Then, eq.(16) writes:

$$s^{\nu-1}\frac{{\rm d}s}{{\rm d}t} = \frac{1}{t_{10}}\left(\frac{\rho}{\rho_J}\right)^{1-2\nu/3}. \tag{19}$$

Here we note that $1 - 2\nu/3 \simeq -0.13$ is a small number. Therefore, the specific entropy of the fluid shows a weak

dependence on the evolution of its density ρ. For a critical density universe we have $\overline{\rho}(t) \propto t^{-2}$, and hence we approximate the solution of eq.(19) by:

$$s^\nu \simeq \int_0^t \nu \left(\frac{\rho}{\rho_J}\right)^{1-2\nu/3} \left(\frac{t'}{t}\right)^{-2(1-2\nu/3)} \frac{\mathrm{d}t'}{t_{10}} \simeq \frac{\nu}{1+2(2\nu/3-1)} \left(\frac{\rho}{\rho_J}\right)^{1-2\nu/3} \frac{t}{t_{10}}, \quad (20)$$

where ρ is the density at the time t we consider. In terms of the temperature-density relation, this yields:

$$T_\alpha(\rho) = T_J \left(\frac{\nu}{1+2(2\nu/3-1)} \frac{t}{t_{10}} \frac{\rho}{\rho_J}\right)^{1/\nu} \quad (21)$$

where we used eq.(18). Thus, the expression (21) gives the first-order term for the expansion of $\ln T$ in terms of the small parameter $(1-2\nu/3)(\mathrm{d}\ln\rho/\mathrm{d}\ln t+2)$. From eq.(16) we note that at $z \lesssim 5$ we have $\rho \sim \rho_J$ and $t_H \sim t_{10}$ hence the temperature of the photo-ionized IGM will be of order $T_J \sim 10^4$ K.

We display in Fig.1 the Equation of State (21) as the solid line which runs through $T \sim 10^4$ K at $\delta = 0$. Beyond the overdensity ρ_c defined in eq.(22) we plot this line as a dashed-line, until it enters the cooling region described in Sect.2.2.1. Indeed, as we explained in Sect.2.2.2 at large densities the "virial temperature" $T_{\rm loc}$ becomes larger than the temperature $T_{\rm ext}$ due to some external energy source (here photo-ionization heating by the UV background radiation). This means that for these regions, which have already reached the non-linear regime as $\delta > \delta_c \sim 5$ (see eq.(22)), shock-heating due to the gravitational dynamics can no longer be neglected and it actually becomes dominant. Therefore, for high densities with $\rho > \rho_c$ the gas should no longer fall onto the curve (21). Nevertheless, since shock-heating can only increase the temperature of the gas the relation (21) now provides a lower bound to the temperature T. Hence, the region below the curve (21) is excluded in the (ρ, T) diagram. This holds until we enter the cooling region discussed in Sect.2.2.1. On the low-density side, as described in Sect.2.2.4 we are constrained by the low-density cutoff $\rho_{-,\rm ext}(T)$.

Therefore, we predict that we should have two phases for the IGM. A first "cool" phase is described by the Equation of State (21) with intermediate densities $\rho_{-,\rm ext} < \rho < \rho_c$. It is photo-ionized gas heated up to $T \sim 10^4$ K by the background UV flux. This corresponds to the moderate density fluctuations which form the Lyman-α forest. A second "warm" phase is made of higher-density regions which have already experienced some shock-heating due to the building of gravitational structures but which have not entered the cooling region yet. These particles should be located in the (ρ, T) plane above the curve (21) and within the constraints described in the previous sections.

2.4. Warm IGM

Thus, the previous discussion shows that a "warm" component of the IGM should no longer follow the equation of state (21) but it remains constrained by the exclusion regions obtained in Sect.2.2. This leaves a closed trapezoidal region in the (ρ, T) plane. Since the temperature of the gas should be governed by the shock-heating due to the gravitational dynamics we can expect a rather large scatter. Indeed, the history of these particles depends on the properties of their neighbouring dark matter density field. This introduces a stochastic component which gives rise to a wide variety of possible histories so that there is no longer a unique temperature-density relation. This agrees well with Fig.11 in Dave et al. (1999) which shows indeed a broad cloud of points in the (ρ, T) plane within the allowed region we obtained in the previous sections.

However, the distribution of matter obtained in Dave et al. (1999) from numerical simulations does not fill entirely this allowed region (note indeed that this is not implied by our previous considerations) and it is not uniform. Hence it would be convenient to derive a curve in the (ρ, T) plane which would describe the "mean" behaviour of this warm phase of the IGM.

To this purpose, we first compute the gas temperature associated with a given halo of mass M which forms at redshift z. Gravitational heating is effective in the collapsing phase of the halo which may be set at $\rho > \rho_c$. One expects ρ_c to be of the order of a few units. We set it to

$$1 + \delta_c = 6 \quad \text{and} \quad \rho_c = (1+\delta_c)\overline{\rho}, \quad (22)$$

which is roughly the value given by the spherical collapse dynamics at turn-around. The collapsing gas then is shock-heated to a temperature of the order of the available kinetic energy, that is to

$$T_{\rm gh} \sim T_{\rm col} \left[\left(\frac{\rho}{\rho_c}\right)^{1/3} - 1\right], \quad (23)$$

with

$$T_{\rm col} = \frac{2}{3}\left(\frac{4\pi}{3}\right)^{1/3} \mu m_p \mathcal{G} M^{2/3} \rho_c^{1/3}, \quad (24)$$

depending on the mass M. The exponent $1/3$ comes from the fact that for a fixed mass M the virial temperature scales as: $T \propto M/R \propto R^{-1} \propto \rho^{1/3}$. The constant term in eq.(23) expresses the fact that gravitational heating comes into play at $\rho > \rho_c$, when non-linear effects appear (e.g., shocks), so that it vanishes at $\rho = \rho_c$. It does not exist for $\rho < \rho_c$. The subscript "gh" refers to the fact that the temperature $T_{\rm gh}$ is governed by "gravitational heating".

For increasing density $\rho > \rho_c$ then, each halo of a given mass M lies on a steeply upwards running curve which originates from this point. These curves show the gravitational heating rapidly dominates over the UV heating, for densities close to ρ_c and temperatures around $T_c = T_\alpha(\rho_c)$. They represent the transition between (eq.(2)) and the fully virialized case (eq.(1)), and have no meaning for

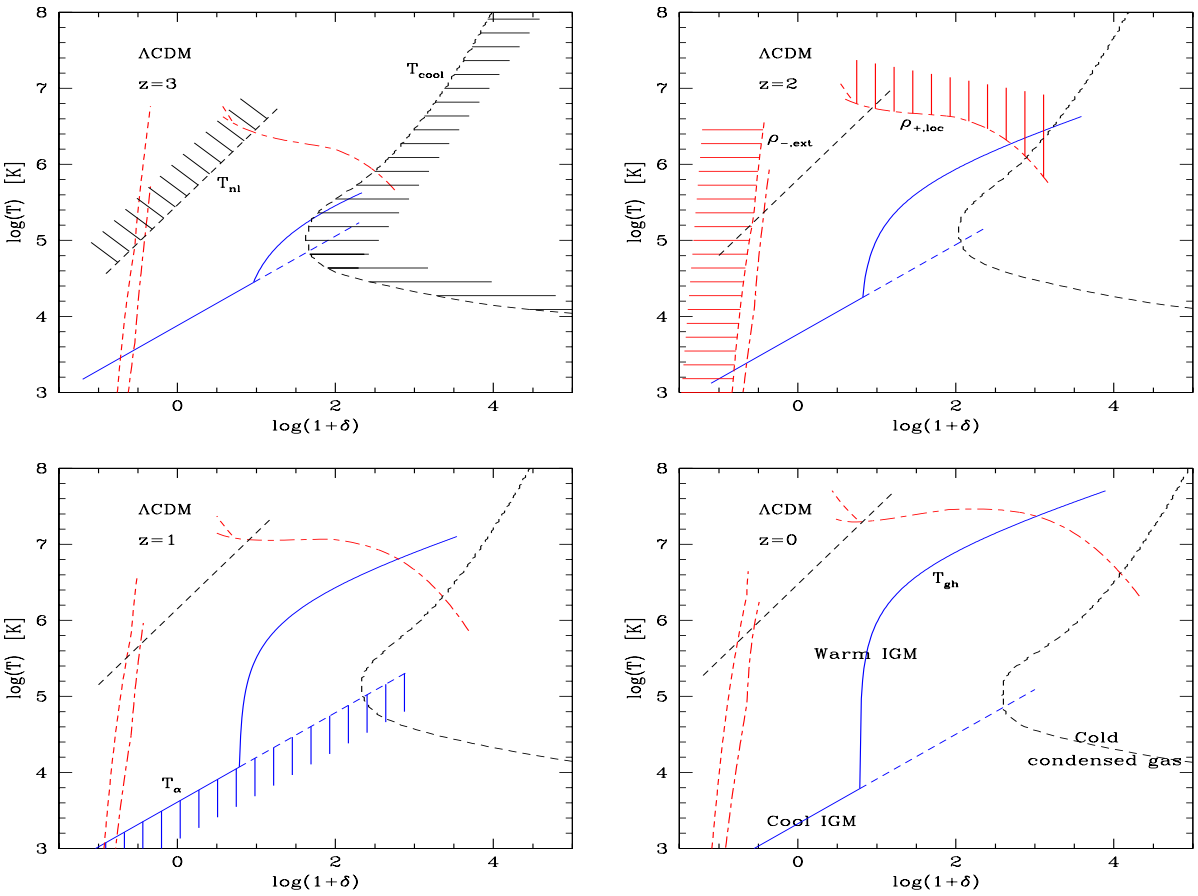

Fig. 1. The phase-diagram of cosmological baryons from $z = 3$ down to $z = 0$. The straight solid line T_α shows the Equation of State of the "cool" IGM (Lyman-α forest). The curved solid line T_{gh} shows, as a mean trend, the "Equation of State" of the "warm" IGM which is shock-heated through the building of non-linear gravitational structures. The dashed curves draw exclusion regions around the allowed domain for this "warm" IGM.

$T_{\rm gh} < T_\alpha(\rho)$ since there is at least the UV heating. There is no reason for these collapsing objects to be the same as the UV heated objects: they actually are, as a rule, different. Note that $T_{\rm gh}$ depends on the characteristic mass M of the object. The mass, as well as the size R of these collapsing objects exhibits a large dispersion in the hierarchical models we consider here. Besides, a more realistic model should include some (moderate) scatter over ρ_c since its unique value would be justified only in the spherical collapse model, which is indeed only a rough approximation. This induces a (rather large) dispersion of the points of the warm IGM in the (ρ, T) plane.

However, for practical purposes we can define an "average" curve which will be the "Equation of State" of the warm IGM, by computing the typical mass $M_{\rm col}(z)$ which collapses at each epoch z. To this purpose we define the length $R_{\rm col}(z)$ by

$$1 + \Delta_c = x_s\, \overline{\xi}(R_{\rm col}, z), \tag{25}$$

where $\Delta_c(z) \sim 177$ is the density contrast of a just-virialized halo as given by the spherical collapse model. The quantity x_s measures the strength of the exponential cutoff at large densities of the pdf $P(\rho_R)$, see eq.(A.10). The relation (25) actually reads $\rho_+(R_{\rm col}) = 1 + \Delta_c$ for small non-linear scales $R_{\rm col}$. This is justified by the fact that we indeed probe non-linear scales, as shown in Fig.1. Thus, the density contrast Δ_c is typical of the halos seen on scale $R_{\rm col}$, which contain most of the matter but occupy a small fraction $\sim 1/\Delta_c$ of the volume. This defines a mass

$$M_{\rm col}(z) = \frac{4\pi}{3}(1 + \Delta_c)\overline{\rho} R_{\rm col}^3, \tag{26}$$

which is the mass that has just turned non-linear at the epoch z. The virial temperature then is obtained through eq.(23). Obviously, the curve (23) used with the mass (26) is only meant to reflect the main trend. Indeed, as discussed above the stochastic character of the dark matter density field leads to a broad variety of (ρ, T) trajectories with time. Nevertheless, the comparison of Fig.1 with Fig.11 in Dave et al. (1999) shows that eq.(23) describes reasonably well the main properties of the "warm" IGM component. A more detailed model which considers the probability distribution of M around $M_{\rm col}(z)$ - this could be done easily along the lines developed in Valageas & Schaeffer (1997)- would also provide the scat-

ter around this mean curve but we shall not tackle this point here. In any case the "warm" IGM should remain enclosed within the allowed region defined by the constraints discussed in the previous sections.

2.5. The different phases of the IGM

Thus, in the previous sections we have described how we could distinguish three components in the baryonic matter of the universe. We have also obtained their location in the (ρ, T) phase-diagram. Our results are displayed in Fig.1.

Firstly, there is a "cool" IGM phase ($T \sim 10^3 - 10^4$ K) which corresponds to the Lyman-α forest. These are moderate density fluctuations ($\delta < \delta_c$) of photo-ionized gas. They are described by the Equation of State (21) which arises from the heating of the gas by the UV background and the cooling due to the expansion (i.e. pressure work). Thus, this component lies on a well-defined curve in the (ρ, T) plane. This curve is bounded towards low densities by the cutoff of the pdf $P(\rho_R)$, which expresses the fact that the dark matter density field arising from Gaussian initial conditions exhibits a finite range of densities which occur with a significant probability. On the other hand, the high-density bound ρ_c is due to gravitational shock-heating which becomes the dominant energy source for dense regions.

Secondly, there is a "warm" IGM phase ($T \sim 10^4 - 10^7$ K) which describes the gas heated by shocks arising from the gravitational energy of just collapsing objects. Because of the stochastic character of this energy source there is a broad scatter for this component around the "Equation of State" we have derived. Nevertheless, this gas is restricted to a specific allowed region in the (ρ, T) phase-diagram. This expresses cooling and heating constraints as well as the properties of the underlying dark matter density field. We also obtained a curve which follows the main trend of this "warm" phase. Its low density bound is set by the transition near ρ_c with the "cool" IGM phase dominated by radiative heating from the UV background. The high-density bound is given by the intersection with the cooling curve (where bremsstrahlung cooling becomes dominant) or the high-density cutoff of the pdf $P(\rho_R)$ (higher densities being very rare). Note that these results are consistent with the calculations of Nath & Silk (2001) based on the Zel'dovich approximation.

Thirdly, some of the "warm" IGM gas may enter the cooling region in the (ρ, T) plane. This gas falls into the potential wells of galactic halos to build stars and a condensed cold component. Some of this gas settles down on the cooling curve at $T \sim 10^4$ K while another part becomes embedded within stars, which we do not study specifically in this paper.

We can note that our results shown in Fig.1 agree with the outcome of numerical simulations as displayed in Fig.11 in Dave et al. (1999) and Fig.9 in Springel & Hernquist (2001).

2.6. Redshift evolution

Finally, the four diagrams displayed in Fig.1 show the evolution with redshift of the properties of the IGM, from $z = 3$ down to $z = 0$. We can see that the overall pattern does not evolve much although the curves exhibit a shift with z. The characteristic temperature of the "cool" IGM decreases slightly with time, in agreement with eq.(21) since the density declines faster than $1/t_H$. Indeed, the cooling rate due to the expansion of the universe scales as $1/t_H$ while the recombination rate (which yields the density of neutral hydrogen involved in radiative heating) scales as ρ. On the other hand, the cooling constraint defined by $t_{\rm c,ef} = t_H$ in Sect.2.2.1 does not evolve much with time. In particular, its lower branch at $T \sim 10^4$ K is set by the atomic physics of hydrogen ionization. Next, the characteristic temperature of the curve $\rho_{+,\rm loc}(T)$ associated with shock-heating due to gravitational clustering grows with time. This expresses the fact that the virial temperature associated with larger scales which turn non-linear later is higher. For instance, the velocity dispersion associated with galaxies is of order ~ 200 km/s while for clusters it is ~ 1000 km/s. Following this evolution, the mean curve $T_{\rm gh}(\rho)$ which describes the "warm" IGM enters the cooling region at high z while at low z it first crosses the high-density threshold $\rho_{+,\rm loc}(T)$. This actually expresses the fact that at high z the collapsed halos built by gravitational clustering form galaxies since the gas undergoes a very efficient cooling, while at low z typical just-virialized halos are clusters which remain hot over a Hubble time and are still strong X-ray emitters (e.g., Valageas & Schaeffer (2000)).

3. Distribution of matter

Thus, in Sect.2 we have discussed how the properties of cosmological baryons could be seen through a (ρ, T) phase-diagram. In particular, we distinguished a "cool" and a "warm" IGM phase. In this section, we derive the fraction of matter enclosed within the "cool" component. As described in Sect.2.3 this corresponds to the Lyman-α forest, that is moderate density fluctuations governed by the ionization and the heating due to the UV background. Since its temperature is not zero this gas probes the dark matter density field over the scale R defined in eq.(2), which describes the length-scale over which pressure can homogenize the baryonic matter distribution. Note that this length depends on the temperature since $R \propto \sqrt{T}$. Then, we wish to express the fraction of matter within the "cool" IGM in terms of the pdf $P(\rho_R)$ over the scales R associated with these clouds. To do so, we first note that these scales are within the non-linear regime as shown by the curve $T_{\rm nl}(\rho)$ in Fig.1 which marks the transition to the linear regime. Then, as discussed in Valageas & Schaeffer (1997), in the highly non-linear regime the pdf $P(\rho_R)$ shows the scaling:

$$P(\rho_R) = \frac{1}{\overline{\xi}^{\,2}}\, h(x) \quad \text{with} \quad x = \frac{\rho_R}{\overline{\rho}}, \tag{27}$$

which defines the scaling function $h(x)$. This holds for densities larger than the low-density cutoffs ρ_- discussed in Sect.2.2.4. Note that if the stable-clustering ansatz is valid this function $h(x)$ does not depend on redshift, as long as one remains in the highly non-linear regime. Then, the fraction of matter enclosed within spherical cells of radius R with a density between the thresholds ρ_1 and ρ_2 is:

$$F_{\rm m} = \int_{\rho_1}^{\rho_2} {\rm d}\rho_R \, \rho_R \, P(\rho_R) = \int_{x_1}^{x_2} \frac{{\rm d}x}{x} \, x^2 h(x). \quad (28)$$

The advantage of the scaling variable x is that the last term in eq.(28) still provides an estimate of the fraction of matter $F_{\rm m}$ associated with a curve (ρ, R) which is not necessarily at constant radius, as discussed in Valageas & Schaeffer (1997). This prediction is compared with numerical simulations in Valageas et al. (2000) where we investigate the two cases of a constant density and a constant radius. Therefore, in order to estimate the fraction of matter associated with the Lyman-α forest we use the variable x and we write:

$$F_{\rm m} \simeq \int \frac{{\rm d}x}{x} \, x^2 h(x, R), \quad (29)$$

with

$$x^2 h(x, R) \equiv \rho_R^2 P(\rho_R, R), \quad (30)$$

where $P(\rho_R, R)$ is the value of the pdf $P(\rho_R)$ at scale R and the integral is taken along the relevant curve (ρ, R). The pdf $P(\rho_R)$ is obtained from eq.(A.2) where the parameter κ which enters eq.(A.5) is computed at the scale R_c associated with the high-density extremity ρ_c of the Equation of State of the Lyman-α forest. Thus, the expression (29) would be exact within the framework described in App.A.1 if the Lyman-α forest were defined by a constant scale R. The use of the variable x in eq.(29) is only meant to handle the fact that R actually varies with ρ.

In order to get an estimate of the error introduced by the fact that we do not integrate along a constant radius we also compute from eq.(29) the fraction of matter not included in this "cool" IGM phase. To do so, we simply integrate eq.(29) along the curve given by eq.(23) which describes the "warm" IGM component. At high z we also include the part which enters the cooling domain in Fig.1. Both mass fractions are displayed by the solid lines in Fig.2. The Lyman-α forest corresponds to the line which grows with redshift and the "warm" IGM to the line which declines at high z. Indeed, at higher z gravitational clustering was less advanced so that a smaller fraction of matter had been shock-heated to high temperatures through the building of large scale structures. The dashed-lines show the same curves normalized so that their sum is unity. As discussed above, the discrepancy comes from the fact that the "objects" we count are not defined by a constant radius. Nevertheless, we see that the correction is rather modest. Moreover, we can check that our results agree reasonably well with the outcome of the numerical simulations described in Dave et al. (1999) (see their Fig.12).

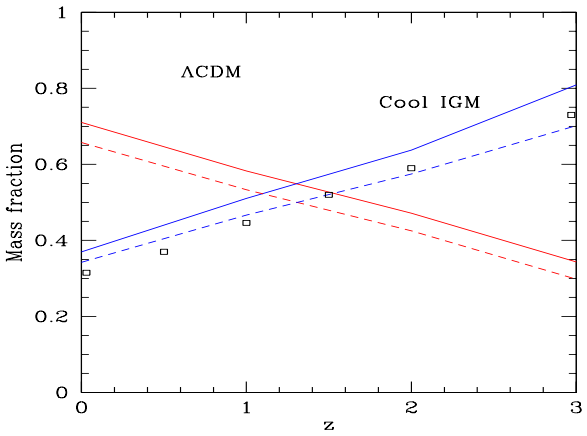

Fig. 2. The distribution of baryonic matter. The solid line which increases with redshift is the fraction of matter within the "cool" IGM phase, as computed from eq.(29) and eq.(21). The solid line which decreases at higher z is the rest of the matter computed from eq.(29) and eq.(23). The dashed-lines are the same curves normalized so that the sum is unity. The squares show the results of the numerical simulations performed in Dave et al. (1999) for the "cool" IGM phase (Fig.12).

4. Warm IGM two-point correlation

Another check on our description of the "warm" IGM component is provided by its two-point correlation function $\xi_{\rm w}(r)$ which measures its spatial clustering. Hence in this section we evaluate $\xi_{\rm w}(r)$, which is defined by:

$$1 + \xi_{\rm w}(\mathbf{r}) \equiv \frac{\langle \rho_{\rm w}(\mathbf{r}_1) \rho_{\rm w}(\mathbf{r}_1 + \mathbf{r}) \rangle}{\langle \rho_{\rm w} \rangle^2}, \quad (31)$$

where $\rho_{\rm w}(\mathbf{r})$ is the density of the "warm" IGM component at point $\mathbf{r}$. In eq.(31) the averages $\langle .. \rangle$ are over the realizations of the density fields or over space (assuming ergodicity). First, from eq.(29) the mean "warm" IGM density is given by:

$$\langle \rho_{\rm w} \rangle = \int \frac{{\rm d}x}{x} x^2 h(x) \frac{\overline{\rho}}{M} V \rho = \overline{\rho} \int \frac{{\rm d}x}{x} x^2 h(x) = \overline{\rho} F_{\rm m,w} \quad (32)$$

where M, R and V are the mass, the radius and the volume associated with the point (ρ, T) in the phase-diagram. The function $h(x)$ is defined as in eq.(30) with the parameter κ computed at the scale R_c. The quantity $F_{\rm m,w}$ is the mass fraction enclosed within the "warm" IGM phase. Note that we always have $\langle \rho_{\rm w} \rangle < \overline{\rho}$ since the "warm" IGM component does not contain all the baryonic matter. Next, the second-order moment is given by:

$$\langle \rho_{\rm w}(\mathbf{r}_1) \rho_{\rm w}(\mathbf{r}_1 + \mathbf{r}) \rangle = \overline{\rho} \int \frac{{\rm d}x_1}{x_1} x_1^2 h(x_1) \rho_{\rm w}(\mathbf{r}, x_1) \quad (33)$$

where $\rho_{\rm w}(\mathbf{r}, x_1)$ is the mean "warm" IGM density at distance $\mathbf{r}$ from a point embedded within the "warm" IGM component with the parameter x_1. Then, as in Valageas et al. (2001a), we write $\rho_{\rm w}(\mathbf{r}, x_1)$ as the sum over two contributions. First, there is a probability $F(r/R_1)$

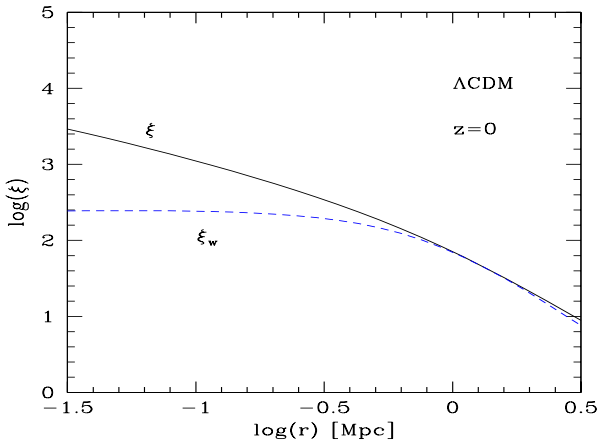

Fig. 3. The "warm" IGM two-point correlation $\xi_{\rm w}(r)$ at redshift $z = 0$ (dashed line). The solid line shows the two-point correlation $\xi(r)$ of the dark matter density field.

that the second point at $\mathbf{r}_1 + \mathbf{r}$ belongs to the same region of radius R_1 of the "warm" IGM. Assuming spherical regions we have:

$$x < 2 : F(x) = 1 - \frac{3x}{4} + \frac{x^3}{16} \quad , \; x > 2 : F(x) = 0. \tag{34}$$

This gives the first contribution $\rho_{\rm w}^{(1)}(\mathbf{r}, x_1)$ as $\rho_{\rm w}^{(1)}(\mathbf{r}, x_1) = \rho_1 F(r/R_1)$. Second, we write the contribution $\rho_{\rm w}^{(2)}(\mathbf{r}, x_1)$ to $\rho_{\rm w}(\mathbf{r}, x_1)$ of other regions of the "warm" IGM component with parameter x_2 as:

$$\rho_{\rm w}^{(2)}(\mathbf{r}, x_1) \; = \; [1 - F(r/R_1)]\, \overline{\rho} \int \frac{{\rm d}x_2}{x_2} x_2^2 h(x_2) \times [1 + b(x_1) b(x_2) \xi(r)] \, . \tag{35}$$

Here $\xi(r)$ is the two-point correlation of the underlying dark matter density field while $b(x_1)b(x_2)$ is the bias associated with the regions x_1 and x_2. This bias is computed from the generating function introduced in eq.(A.2) as described in Bernardeau & Schaeffer (1992) (see also Valageas et al. (2001b) for a comparison with observations). Thus, we write the second-order moment as:

$$\langle \rho_{\rm w}(\mathbf{r}_1) \rho_{\rm w}(\mathbf{r}_1 + \mathbf{r}) \rangle = \overline{\rho}^2 \int \frac{{\rm d}x_1}{x_1} x_1^2 h(x_1) \Big\{ \rho_{R1} F(r/R_1) + (1 - F(r/R_1)) \int \frac{{\rm d}x_2}{x_2} x_2^2 h(x_2) \, [1 + b(x_1) b(x_2) \xi(r)] \Big\} \tag{36}$$

This yields the "warm" IGM two-point correlation $\xi_{\rm w}(r)$ through eq.(31).

We show our result at $z = 0$ in Fig.3. On large scales the "warm" IGM correlation is close to the dark matter correlation because i) we assumed that baryonic matter follows the dark matter density field smoothed over the scale R which describes the processes at work (R is set by the location on the (ρ, T) plane) and ii) the "warm" IGM component is mainly made of typical density fluctuations. This is seen by the fact that, by definition, most of its matter is within the allowed region in the (ρ, T) phase-diagram, below the high-density cutoff $\rho_{+,{\rm loc}}(T)$. This implies that the biases which enter the expression (36) are close to unity since we do not select rare high densities or voids by looking at the "warm" IGM phase. On the other hand, at small scales $r \lesssim 300$ kpc the two-point correlation function $\xi_{\rm w}(r)$ flattens and it reaches a finite limit at $r = 0$. This expresses the fact that the non-zero temperature of the gas reached by shock-heating ($T > 10^4$ K) gives rise to pressure effects which homogenize the baryonic distribution over some scale R. A lower limit to this length R is set by the scale R_c associated with the critical point (ρ_c, T_c) in the phase-diagram. Indeed, as shown by the curved solid line in Fig.1, at redshift $z = 0$ the length scales associated with the "warm" IGM run from R_c up to scales of order R_0 which are turning non-linear. This sets the knee of the two-point correlation $\xi_{\rm w}(r)$ at $r \sim 300$ kpc at $z = 0$. On the other hand, the value at $r = 0$ yields the clumping factor $C_{\rm w}$ which we define by:

$$C_{\rm w} \equiv \frac{\langle \rho_{\rm w}^2 \rangle}{\langle \rho_{\rm w} \rangle^2} = 1 + \xi_{\rm w}(0). \tag{37}$$

We obtain $C_{\rm w} \simeq 230$ at $z = 0$. Finally, we can check that our results agree with the outcome of the numerical simulations described in Dave et al. (2001) (see their Fig.7). In particular, we recover the knee at $r \sim 300$ kpc and a reasonable value for the clumping factor $C_{\rm w}$.

5. Soft X-ray background

Finally, we check in this section whether the soft X-ray background emitted by the "warm" IGM in our model is consistent with observations. Experiments show that the extragalactic soft X-ray background flux in the $0.1 - 0.4$ keV band is of order $20 - 35$ keV cm^{-2} s^{-1} sr^{-1} keV^{-1} (e.g., Warwick & Roberts (1998)). However, most of this flux is due to AGN so that the contribution from diffuse gas should obey the constraint $F_\nu \lesssim 4$ keV cm^{-2} s^{-1} sr^{-1} keV^{-1} in this frequency range (e.g., see the discussion in Wu et al. (2001)). Using the Press-Schechter formalism (Press & Schechter (1974)), assuming that the X-ray emitting gas is embedded within just-virialized halos with a density contrast $\Delta_c(z) \gtrsim 177$, some previous studies obtained a flux which is higher than this upper bound (e.g., Pen (1999), Wu et al. (2001)). This led these authors to infer that a non-gravitational heating source is needed to unbind the gas from groups and small clusters in order to reduce their contribution to the soft X-ray background. However, a large fraction of the gas is actually part of the "warm" IGM component, within filamentary structures at density contrasts lower than $\Delta_c(z)$. Then, this gives a smaller X-ray background since the X-ray emission is proportional to the squared density of the gas. As argued in Dave et al. (2001) this reduced X-ray background could then be consistent with observational constraints.

Therefore, we compute here the soft X-ray background due to the diffuse "warm" IGM phase, in the $0.1 - 0.4$ keV

band. The X-ray flux $F_{\nu_1-\nu_2}$ within this frequency band can be written:

$$F_{\nu_1-\nu_2} = 7.13\times10^{-34}\mathrm{keV\ cm^{-2}\ s^{-1}\ sr^{-1}} \times \int \mathrm{d}z\ c\frac{\mathrm{d}t}{\mathrm{d}z}(1+z)^2 \int \frac{\mathrm{d}x}{x}x^2h(x)(1+\delta)T^{1/2} \times \left(e^{-h\nu_1(1+z)/(kT)} - e^{-h\nu_2(1+z)/(kT)}\right), \quad (38)$$

where the temperature T is in Kelvin units. Here we used eq.(29) which states that the fraction of matter associated with the interval $\mathrm{d}x$ along the curve $T_{\rm gh}(\rho)$ in the (ρ,T) plane is $\mathrm{d}F_{\rm m} \simeq xh(x)\mathrm{d}x$. The factor $(1+\delta)$ in eq.(38) comes from the fact that the X-ray emission is proportional to the squared density n_e^2. The integral over x in eq.(38) follows the curve $T_{\rm gh}(\rho)$, from eq.(23), in the (ρ,T) phase-diagram. Its lower-density bound is given by the threshold ρ_c introduced in eq.(22) while its upper-density bound is set by the intersection with the cooling curve defined by eq.(4). Indeed, at higher densities the gas enters the cooling region so that it no longer emits in X-rays. Moreover, it corresponds to collapsed halos which form discrete galaxies. Then, our calculation gives an X-ray background flux $F_{\nu_1-\nu_2} = 0.93$ keV cm^{-2} s^{-1} sr^{-1} in the $0.1-0.4$ keV band. This yields a mean differential flux $F_\nu = 3.1$ keV cm^{-2} s^{-1} sr^{-1} keV^{-1} in this band. Thus, we can check that our result is consistent with observations. It is close to the observational upper bound which means that the "warm" IGM component might be observable through its X-ray emission in the near future.

6. Conclusion

In this article we have shown that the (ρ,T) phase-diagram of cosmological baryons can be understood in very simple terms. It is strongly model-independent since the relevant scales are set by atomic physics (hydrogen ionization) and the basic cosmological setting (the rate of expansion and the scale which marks the transition to the non-linear regime). Then, we have distinguished three components. Firstly, a "cool" IGM phase corresponding the Lyman-α forest follows a well-defined Equation of State on the (ρ,T) plane. We have shown that the properties of this gas do not depend much on its previous history because of the form of the recombination coefficient. This explains why the scatter of this component obtained in numerical simulations is quite small. Secondly, a "warm" IGM phase is formed by the gas which has been shock-heated to large temperatures $T\sim10^4-10^7$ K as non-linear gravitational structures appear. The dependence on the stochastic gravitational potential entails a broad scatter in the (ρ,T) plane. However, we have explained that robust constraints only allow a closed region in the (ρ,T) phase-diagram for this component. We have also defined a simple curve which represents its mean behaviour and plays the role of the warm IGM Equation of State. The warm IGM is seen to be due to objects on their way of collapsing under the action of gravity.. The hot gas which lies within clusters and galactic halos simply corresponds to the high-density part of this curve (e.g., $\delta\gtrsim200$). Thirdly, we find two quite different regimes for the warm IGM. At high redshift, some of the "warm" component enters the cooling region of the (ρ,T) plane: this gives rise to galactic disks and stars. Some of this matter should lie on the low temperature branch of this cooling region, in agreement with the results of numerical simulations (Dave et al. (1999)). At low redshift, the warm IGM no longer lies within the cooled region, and it is at the origin of the hot gas in clusters. So, the evolution with redshift of the phase-diagram provides a natural confirmation that at high z collapsed halos form galaxies while at low redshift ($z\lesssim1$) they build groups or clusters.

Then, we have checked that our results for the fraction of matter enclosed within the "cool" IGM phase and the two-point correlation function of the "warm" IGM component agree with numerical simulations (e.g., Dave et al. (1999) and Dave et al. (2001)). This confirms the validity of our analysis. Note however that the latter relies on simple physical considerations and it is independent of the findings of the former. Besides, the soft X-ray background due to the "warm" IGM is consistent with the upper bound set by observations. Our prediction actually is close to the observational limit: this offers the prospect of measuring this X-ray emission in future observations.

Appendix A: Dark matter density field

In this appendix we describe the analytic procedure we use to model the dark matter density field. Our method provides a simple means to estimate the pdf of the density contrast from the quasi-linear up to the highly non-linear regime, parameterized by only one variable (the skewness). This should be sufficient for our purpose which is merely to obtain the main properties of the IGM. Note that by construction the variance and the skewness of the pdf we obtain below agree with the results of numerical simulations, in both the quasi-linear and the highly non-linear regimes.

A.1. The pdf $P(\rho_R)$ of the overdensity at scale R

First, we note $\overline{\xi}$ the moment of order two of the density contrast δ_R over a spherical cell of radius R and volume V. It can be expressed in terms of the two-point correlation function $\xi(\mathbf{x}_1,\mathbf{x}_2)=\xi(|\mathbf{x}_1-\mathbf{x}_2|)$ as:

$$\overline{\xi} \equiv \langle\delta_R^2\rangle = \int_V \frac{\mathrm{d}\mathbf{x}_1\mathrm{d}\mathbf{x}_2}{V^2}\ \xi(\mathbf{x}_1,\mathbf{x}_2). \quad (A.1)$$

The two-point correlation $\xi(x)$ is the Fourier transform of the non-linear power-spectrum $P(k)$ which we compute from the linear power-spectrum $P_L(k)$ using the analytic formulae obtained by Peacock & Dodds (1996) from fits to N-body simulations. Of course, in the quasi-linear limit $\overline{\xi}\to0$ we have $\overline{\xi}=\sigma^2$. Then, it is convenient to intro-

duce the generating function $\varphi(y)$ defined by the inverse Laplace transform:

$$P(\rho_R) \equiv \int_{-i\infty}^{+i\infty} \frac{\mathrm{d}y}{2\pi i\overline{\xi}}\, e^{[\rho_R y-\varphi(y)]/\overline{\xi}}, \tag{A.2}$$

where $P(\rho_R)$ is the pdf of the overdensity over a cell of radius R:

$$\rho_R \equiv 1+\delta_R. \tag{A.3}$$

The advantage of the generating function $\varphi(y)$ is that it reaches a finite limit in the quasi-linear regime $\overline{\xi} \ll 1$. Moreover, in this regime one can derive $\varphi(y)$ in a rigorous manner from the equations of motion (Bernardeau (1992,1994), Valageas (2001)). On the other hand, in the highly non-linear regime $\overline{\xi} \gg 1$ the generating function $\varphi(y)$ should also reach a finite (astonishingly close to the former, but seemingly not identical) limit if the stable-clustering ansatz is valid (Balian & Schaeffer (1989)). This is seen to agree reasonably well with the results of numerical simulations (e.g., Valageas et al. (2000)). Therefore, hereafter we use the following simple parameterization for the generating function $\varphi(y)$:

$$\left\{ \begin{array}{l} \tau = -y\,\zeta'(\tau) \\ \\ \varphi(y) = y\,\zeta(\tau) + \dfrac{\tau^2}{2} \end{array} \right. \tag{A.4}$$

with:

$$\zeta(\tau) \equiv \left(1+\frac{\tau}{\kappa}\right)^{-\kappa}. \tag{A.5}$$

This yields a family of functions $\varphi(y)$ which depends only on the parameter κ.

Such a relationship arises naturally in the exact derivation of $\varphi(y)$ in the quasi-linear limit (Bernardeau (1992,1994), Valageas (2001)). Besides, it also appears in the non-linear regime within the framework of the "minimal tree-model" (Bernardeau & Schaeffer (1992), Schaeffer (1985)). It can be seen that the phenomenological form (A.5) for $\zeta(\tau)$ also yields reasonable results.

As in Bernardeau & Valageas (2000), we choose the parameter κ which enters eq.(A.5) so as to recover the skewness $S_3 \equiv \langle\delta_R^3\rangle_c/\overline{\xi}^2$ predicted by HEPT (Scoccimarro & Frieman (1999)) in the non-linear regime. More precisely, we use:

$$\overline{\xi}<0.1:\ S_3=\frac{34}{7}-(n+3),\ \ \overline{\xi}>10:\ S_3=\frac{3(4-2^n)}{1+2^{n+1}} \tag{A.6}$$

and we interpolate between both values in the range $0.1 < \overline{\xi} < 10$. Here we note n the slope of the linear-power spectrum at the scale of interest. Note that this procedure was seen in Bernardeau & Valageas (2000) to match the results of numerical simulations with respect to weak gravitational lensing effects. Therefore, it should be quite sufficient for our present purpose which is mainly to investigate the main trends of the IGM properties.

A.2. High and low density cutoffs $\rho_\pm(R)$

Now, we can estimate the high and low density cutoffs $\rho_\pm(R)$ of the pdf $P(\rho_R)$ as follows. To each overdensity ρ_R we associate the Laplace variable $y_c(\rho_R)$ (and τ_c through eq.(A.4)) defined as the saddle-point of the exponent in eq.(A.2). This can be written:

$$\rho_R \equiv \varphi'(y_c) = \zeta(\tau_c), \tag{A.7}$$

where we used eq.(A.4) to derive the last equality. Note that δ_R and the pair (y_c,τ_c) are of opposite signs. The reason for the introduction of y_c is that for extreme overdensities $\rho_R \to \infty$ or $\rho_R \to 0$, that is in the tails of the pdf $P(\rho_R)$, the integral (A.2) is dominated by the contribution from $y \simeq y_c$ (e.g., Balian & Schaeffer (1989)). Then, it is clear that the density cutoffs of the pdf are given by the points $\rho_\pm$ where the argument of the exponential in eq.(A.2) at the saddle-point is of order unity and negative (note that it is zero at the mean overdensity $\langle\rho_R\rangle = 1$). Indeed, for larger $|\delta_R|$ the argument becomes more negative than -1 which leads to the exponential falloffs of $P(\rho_R)$. Therefore, we define the high and low density cutoffs $\rho_\pm$ by the condition:

$$\frac{\rho_\pm y_c - \varphi(y_c)}{\overline{\xi}} = -1, \tag{A.8}$$

where $y_c = y_c(\rho_\pm)$ as given by eq.(A.7). This relation can be most conveniently written in terms of the variable τ which yields:

$$\tau_\pm = \mp\sqrt{2\overline{\xi}} \tag{A.9}$$

where we used eq.(A.5). In the highly non-linear regime eq.(A.9) yields $\tau_+ \ll -1$. However, as discussed in Bernardeau & Schaeffer (1992) the implicit system (A.4) is singular at a finite value $\tau_s = -\kappa/(2+\kappa)$ which leads to an exponential tail for the pdf $P(\rho_R) \sim e^{-\rho_R/(x_s\overline{\xi})}$. Hence for $-\sqrt{2\overline{\xi}} < \tau_s$ we take $\tau_+ = \tau_s$ and $\rho_+ = x_s\overline{\xi}$. Thus, we obtain for the high-density cutoff $\rho_+(R)$:

$$\overline{\xi}\ll 1:\ \rho_+ = 1+\sqrt{2\overline{\xi}},\quad \overline{\xi}\gg 1:\ \rho_+ = x_s\overline{\xi} \tag{A.10}$$

and for the low-density cutoff $\rho_-(R)$:

$$\overline{\xi}\ll 1:\ \rho_- = 1-\sqrt{2\overline{\xi}},\quad \overline{\xi}\gg 1:\ \rho_- \sim \overline{\xi}^{\,-\kappa/2}. \tag{A.11}$$

Note that in the quasi-linear regime we recover $|\delta_\pm| \sim \sqrt{\overline{\xi}} = \sigma$ as required for Gaussian initial conditions. Then, the density cutoffs $\rho_\pm$ are close to the mean: $\rho_\pm \sim \langle\rho_R\rangle = 1$ for $\overline{\xi} \ll 1$. On the other hand, in the highly non-linear regime the cutoffs are displaced to very low densities ($\rho_- \ll 1$: rare voids) and high densities ($\rho_+ \gg 1$: collapsed halos).

References

Anninos, P., Zhang, Y., Abel, T., Norman, M.L., 1997, NewA 2, 209

Balian, R., Schaeffer, R., 1989, A&A 220, 1
Bernardeau, F., 1992, ApJ 392, 1
Bernardeau, F., 1994, A&A 291, 697
Bernardeau, F., Schaeffer, R., 1992, A&A 255, 1
Bernardeau, F., Valageas, P., 2000, A&A 364, 1
Cen, R., Ostriker, J.P., 1999, ApJ 514, 1
Cooke A.J., Espey B., Carswell R.F., 1997, MNRAS 284, 552
Dave, R., Hernquist, L., Katz, N., Weinberg, D.H., 1999, ApJ 511, 521
Dave, R., Cen, R., Ostriker, J.P., et al., 2001, ApJ 552, 473
Fukugita, M., Hogan, C.J., Peebles, P.J.E., 1998, ApJ 503, 518
Giallongo E., Cristiani S., D'Odorico S., Fontana A., Savaglio S., 1996, ApJ 466, 46
Hui, L., Gnedin, N.Y., 1997, MNRAS 292, 27
Nath, B.B., Silk, J., 2001, submitted to MNRAS, astro-ph/0107394
Peacock, J.A., Dodds, S.J., 1996, MNRAS 280, L19
Pen, U.-L., 1999, ApJ 510, L1
Press, W.H., Schechter, P., 1974, ApJ 187, 425
Rees, M.J., Ostriker, J.P., 1977, MNRAS 179, 541
Scoccimarro R., Frieman J.A., 1999, ApJ 520, 35
Schaeffer, R., 1985, A&A 144, L1
Silk, J., 1977, ApJ 211, 638
Springel, V., Hernquist, L., 2001, submitted to MNRAS, astro-ph/0111016
Tytler, D., O'Meara, J.M., Suzuki, N., Lubin, D., 2000, Physica Scripta T 85, 12
Valageas, P., 2001, submitted to A&A, astro-ph/0107126
Valageas, P., Balbi, A., Silk, J., 2001, A&A 367, 1
Valageas, P., Lacey, C., Schaeffer, R., 2000, MNRAS 311, 234
Valageas, P., Schaeffer, R., 1997, A&A 328, 435
Valageas, P., Schaeffer, R., 1999, A&A 345, 329
Valageas, P., Schaeffer, R., 2000, A&A 359, 821
Valageas, P., Schaeffer, R., Silk, J., 1999, A&A 345, 691
Valageas, P., Schaeffer, R., Silk, J., 2001, A&A 366, 363
Vogel S.N., Weymann R., Rauch M., Hamilton T., 1995, ApJ 441, 162
Warwick, R.S., Roberts, T.P., 1998, Astronomische Nachrichten, 319, 59
Wu, K.K.S., Fabian, A.C., Nulsen, P.E.J., 2001, MNRAS 324, 95
Zel'dovich, Ya. B., 1970, A&A 5, 84